



Size Dependence of Transport Non-Uniformities on Localized Plating in Lithium-Ion Batteries

Xinyi M. Liu, Alta Fang, Mikko P. Haataja, and Craig B. Arnold *,^z

Department of Mechanical and Aerospace Engineering, Princeton Institute for the Science and Technology of Materials, Princeton University, Princeton, New Jersey 08544, USA

Plating in lithium-ion batteries not only reduces their lifetime, but also raises safety concerns. Preventing metallic lithium from forming is difficult, as the heterogeneity of materials typically used in batteries can create transport non-uniformities, which can lead to unanticipated local plating. Therefore, being able to predict the occurrence of plating due to a non-uniformity of a certain shape and size becomes essential. In this study, we probe the importance of the size scale and geometry on localized plating through numerical simulations and experiments. Using modified separators to create transport non-uniformities, we show that certain geometric features lead to more vulnerability to plating, and localization strongly depends on size. A single large feature in a separator induces more plating than a collection of smaller features with same total area. Our findings help elucidate the fundamentals behind heterogeneous plating, which can provide practical insights into battery safety and product control.

© The Author(s) 2018. Published by ECS. This is an open access article distributed under the terms of the Creative Commons Attribution 4.0 License (CC BY, <http://creativecommons.org/licenses/by/4.0/>), which permits unrestricted reuse of the work in any medium, provided the original work is properly cited. [DOI: [10.1149/2.1181805jes](https://doi.org/10.1149/2.1181805jes)]



Manuscript submitted February 26, 2018; revised manuscript received March 26, 2018. Published April 17, 2018.

Lithium-ion batteries are widely used in many applications, but extending battery life and improving battery safety still remain challenging. The massive use of batteries in electric vehicles and other devices that require fast charging has made battery safety an even more important issue. Among all the side reactions and degradation mechanisms, lithium plating, which is the deposition of metallic lithium on the electrode surface, is one of the most dangerous.¹⁻³ The plated lithium can grow in the form of dendrites, which may pierce through the separator and lead to a short circuit.^{4,5} Although it remains challenging to prevent metallic lithium from forming, progress has been made to unveil the complicated plating mechanism. Plating usually occurs under a high charging rate or at a low temperature, when the amount of lithium ions arriving at the negative electrode surface exceeds the amount of lithium ions that can be intercalated.⁶⁻⁸ If the local overpotential of the lithium deposition reaction drops below 0 V vs. Li/Li⁺, it becomes thermodynamically favorable for metallic lithium to form, which is a widely adopted criterion for lithium plating.^{9,10}

While most lithium plating can be avoided if the battery is cycled under normal working conditions, it is hard to prevent localized plating and even harder to detect a small amount.¹¹⁻¹⁴ Localized plating can occur due to heterogeneities inside batteries which can be caused by faults in cell manufacturing, bad contact between electrodes and current collectors, gas bubbles, or other non-uniformities that either pre-exist or arise during cycling.¹⁵⁻¹⁷ For instance, heterogeneous compression of the cell creates regions with local high mechanical stresses, which lead to plating and accelerated capacity loss.^{17,18} Besides external stresses, any variations in layer thicknesses can cause non-uniform internal stress in the separator, changing its porosity, which affects the ionic conductivity.^{15,19-21} For instance, a 5±1 μm thick separator can develop an internal strain of 20% even without any external stress applied. Therefore, being able to predict whether a certain heterogeneity would cause undesirable battery degradation becomes extremely important.

This work builds on our previous paper in which we established a correlation between defects in separators and localized plating.¹⁵ Using an axisymmetric shape of defect, Cannarella, et al. demonstrated experimentally and numerically that pore closure in separators causes non-uniform ion flow, resulting in regions with high current densities, thus inducing plating. However, that work was limited in its ability to quantify the effects of pore closure shape as well as the size. In this work we extend the defect to include non-axisymmetric shapes in order to study localization around various geometries, as well as

experimentally quantify the critical defect size. Building on previous models, we make simplifications and develop a fully 3D model that is computationally fast while remaining able to predict plating locations. By studying various geometries, we show that plating preferentially occurs in regions where the amount of blocked ions is large compared to the available exit in that region. We also demonstrate that localization strongly depends on defect size and at a constant current density, there exists a critical size below which localization is greatly reduced. We find that it is the maximum size of an individual defect rather than the overall defect area that dictates plating.

Experimental Methods

We define the term *defect* to mean a region of non-uniformity that has different ionic transport properties than other regions. Here we use this term to describe a general ionic transport scenario that can be caused by a deficiency in any of the cell components, instead of a material fault or a defect in its traditional meaning. Depending on the defect shape, the critical size of the defect can be described in terms of length, radius, or area. For instance, for a set of rectangular regions with the same length but different widths, defect size can be characterized by the width of the region. In the past, we have experimentally created transport heterogeneities by mechanically compressing separators to cause pore closure.¹⁵ Here, we use similar techniques to create separator defects with various shapes and sizes.

To create transport non-uniformities, separator defects were carefully introduced inside cells. A 7 μm-thick commercial separator obtained from Sempcorp Co. was compressed under an Instron machine at 200 MPa for 20 minutes. This process allowed the pores to collapse, which resulted in a color change from white to partially transparent, and with an average final thickness of 3 μm.²² The thin 7 μm separator was chosen to minimize the effects caused by differences in layer thickness due to the inclusion of the defect. The mechanical compression results in pore closure, which significantly decreases the ion transport in the assembled cell.²³

The compressed separator was then cut into specific shapes and designs using a laser and was carefully transferred into a glove box. In this work, we chose designs of an isosceles triangle with two 75-degree vertices and an M shape as shown in Figure 1. The asymmetries of these two structures allow us to study the localization effects for various shapes, such as edges, corners, and vertices. We also cut the compressed separators into rectangular stripes with width ranging from 50 μm to 1 mm. Upon assembly, the compressed separator was placed in between the negative electrode and a pristine layer of separator (Celgard 3501), which has a nominal thickness of 25 μm. Figure 2a shows a schematic of the cell assembly. Electrodes were harvested

*Electrochemical Society Member.

^zE-mail: cbarnold@Princeton.EDU

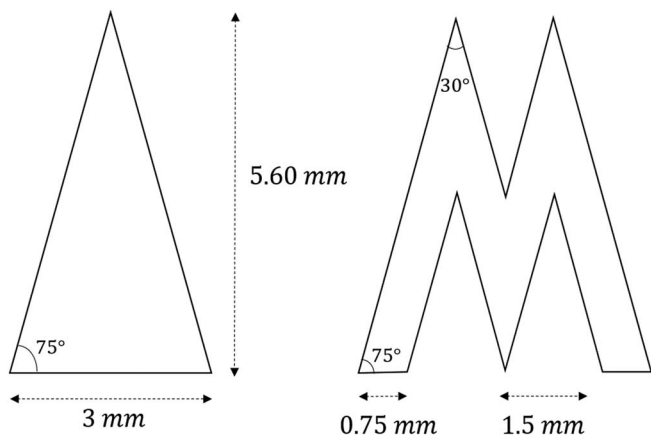


Figure 1. Geometry and dimensions of two separator defect designs.

from commercial pristine pouch cells (C/LCO) and were presoaked with electrolyte before assembly. Excess electrolyte was used and each cell was allowed to sit for 12 hours to ensure that electrodes and separators were fully wet.

Here we define the total area of defects to be $A_{d,total}$. With a total number of n defects,

$$A_{d,total} = A_1 + A_2 + A_3 + \dots + A_n \quad [1]$$

and the area of the largest defect is $A_{d,max}$, represented as

$$A_{d,max} = \max_{1 \leq i \leq n} \{A_i\}. \quad [2]$$

If all n defects have the same area,

$$A_{d,total} = nA_i. \quad [3]$$

Here, the applied current was adjusted based on the active area, so that the average current density was the same across all cells. Cells were cycled under constant current constant voltage (CCCV) charging between 3 V and 4.2 V, with a cut off current at C/10. The applied current i_{app} is calculated as the current applied on a cell with no defect times a correction factor f :

$$i_{app} = i_{pristine} \times f \quad [4]$$

and

$$f = \frac{A_{cell} - A_{d,total}}{A_{cell}} \quad [5]$$

where A_{cell} is the total cross-sectional area. Here $i_{pristine}$ was chosen to correspond to a cycling rate of 0.67 C, because 0.67 C is below the plating threshold while also high enough to accelerate the tests. After cycling, cells were disassembled inside an Argon-filled glove box at a

state of charge of zero, and images of the graphite electrodes were immediately recorded using a wireless camera.

Modeling Methods

In this section we develop a simplified model that can be used to predict locations of localized plating and help experimental design. Beginning with the full governing equations of a porous electrode model, which is described in Refs. 15, 24, 25, we make several simplifying assumptions to reduce the required computational expense of simulations. Our aim here is not to make quantitative predictions about particular battery cells but rather to provide physical insight that can help inspire experimental designs and explain experimental observations.

We begin with Newman's porous electrode model for lithium-ion batteries, which uses volume-averaged continuous fields to model the complex interconnected network of solid particles and liquid electrolyte comprising the porous electrodes.^{15,24,25} The first simplification we make is to neglect lithium concentration gradients within each of the solid-phase particles in the electrodes, which corresponds to assuming that the current densities and electrode particles are small enough that the diffusion length inside the electrode solid particles is much larger than the particle radius.²⁴ This assumption allows us to remove an entire pseudo dimension of the electrode particles and greatly reduces the complexity of the model. Secondly, we assume that the solid-phase potential in each electrode is constant, since the electronic conductivity of the solid phase is significantly higher than that of the electrolyte.^{10,15,26} Next, we assume that the Butler-Volmer equation can be linearized, which is a reasonable assumption for low overpotentials.¹⁰ Finally, we assume a constant electrolyte concentration, which corresponds to assuming a cation transference number of one.²⁷ We believe this assumption should not affect our qualitative results, since our model accounts for ion transport via migration, and accounting for diffusion effects due to a lower cation transference number would simply lead to further ion transport limitations. These assumptions result in the following simplified model where the only remaining spatially varying unknowns to solve for are the solid-phase lithium concentration $c_s(\vec{r}, t)$ in the electrodes and the liquid-phase potential $\phi_2(\vec{r}, t)$ throughout the cell. Figure 2b shows a schematic of the cell cross section used in the model, where the gray area represents a defect region that has pore closure. The thickness of the defect does not change the overall plating behaviors. Therefore, for simplicity, the defect region has been extended all the way from the anode to the cathode in the model.

After simplifying, the governing equations in the electrodes are:

$$\varepsilon_s \frac{\partial c_s}{\partial t} = -aj; \quad [6]$$

$$j\mathcal{F} = i_0(c, c_s, k) \frac{\mathcal{F}}{RT} (\phi_1 - \phi_2 - U(c_s)). \quad [7]$$

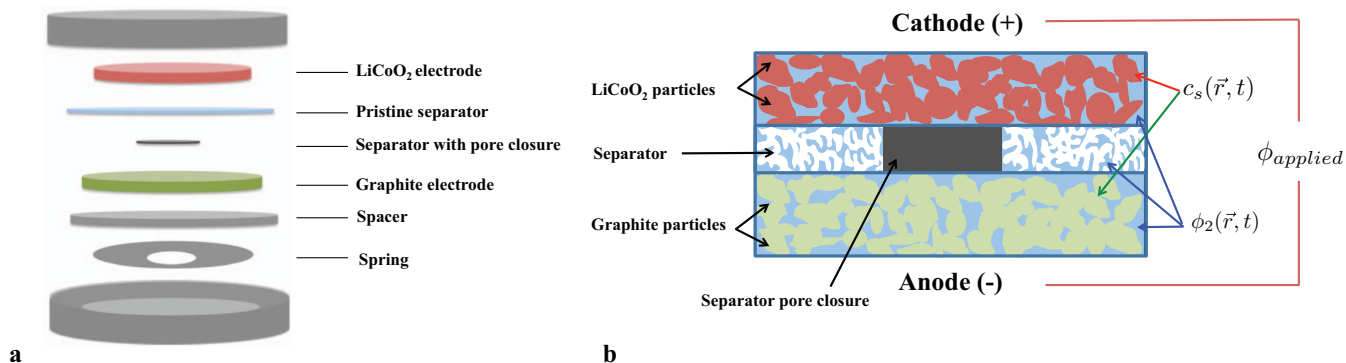


Figure 2. (a) A schematic of a lithium-ion coin cell assembly. (b) Model schematic of a cell cross section showing a porous cathode, porous battery separator with a region of pore closure, and porous anode immersed in the liquid electrolyte.

Table I. Symbols in the lithium-ion battery model.

Symbol	Parameter	Value	Units		
T	temperature	298	K		
\mathcal{F}	Faraday's constant	96485	C/mol		
R	universal gas constant	8.31	J/mol K		
κ	bulk ionic conductivity	1.2	S/m		
c	electrolyte concentration	1000	mol/m ³		
ϕ_2	liquid-phase potential	variable	V		
j	pore wall flux	variable	$\frac{\text{mol}}{\text{m}^2\text{s}}$		
Symbol	Parameter	Anode	Separator	Cathode	Units
L	thickness	7.37×10^{-5}	2.46×10^{-5}	7.02×10^{-5}	m
ϵ_l	volume fraction liquid	0.438	0.45	0.3	–
ϵ_s	volume fraction solid-phase	0.505	–	0.55	–
$brug$	Bruggemann exponent	4.1	2.3	1.5	–
k	rate constant	4.9×10^{-11}	–	2.8×10^{-10}	$\frac{\text{m}^{2.5}}{\text{mol}^{0.5}\text{s}}$
a	specific interfacial area	1.2×10^5	–	1.9×10^5	1/m
$c_{s,max}$	maximum solid-phase Li concentration	30540	–	56250	mol/m ³
$c_{s,min}$	minimum solid-phase Li concentration	0	–	20976	mol/m ³
$c_s(t=0)$	initial solid-phase Li concentration	305.4	–	54562.5	mol/m ³
ϕ_1	solid-phase potential	$-\phi_{applied}$	–	0	V

Equation 6 is a simplified form of the continuity equation that relates the concentration of lithium in the electrode to the flux at the electrode surface, where c_s is the lithium concentration in the electrode solid particles and j is the lithium ion flux at the particle-electrolyte interface. The volume fraction ϵ_s and specific interfacial area a are model parameters whose values are listed in Table I. The flux at the surface can be related to the overpotential through the linearized Butler-Volmer equation, Equation 7, where i_0 is the concentration-dependent exchange current density, and $\phi_1 - \phi_2 - U(c_s)$ is the insertion reaction overpotential. The following two equations are used to model lithium ion transport in the liquid phase within the electrodes and within the separator respectively:

$$aj\mathcal{F} = \vec{\nabla} \cdot (-\kappa_{eff} \vec{\nabla} \phi_2); \quad [8]$$

$$0 = \vec{\nabla} \cdot (\kappa_{eff} \vec{\nabla} \phi_2). \quad [9]$$

The effective conductivities κ_{eff} in the electrodes and separator depend on the porosity and the Bruggeman exponent. To simulate the pore closure region where the pathway of lithium ion conduction is completely blocked, we set κ_{eff} in the pore closure region to be significantly smaller than that in the pristine region and multiply κ_{eff} by 1×10^{-6} .

The parameter values shown in Table I are taken from Refs. 15 and 10, which correspond to a lithium-ion battery with a graphite anode and LCO cathode. After applying the boundary conditions at the edge and at the pore closure, we numerically solve the equations by first solving for ϕ_2 and then using explicit Euler time stepping to evolve c_s . The following two expressions will be used to determine the local state of charge and the local potential in the anode, which are characterized as

$$SOC = \frac{c_s - c_{s,min}}{c_{s,max} - c_{s,min}}; \quad [10]$$

$$V_- = \phi_{1,-} - \phi_2 = -\phi_{applied} - \phi_2. \quad [11]$$

The local potential in the anode with respect to a lithium reference electrode, V_- , is equal to the difference between the local solid-phase potential $\phi_{1,-}$ and liquid-phase potential ϕ_2 . A negative value of V_- indicates that lithium plating is thermodynamically favorable.

Localization and Defect Geometry

Certain locations around a defect are more vulnerable to plating than others. In the case of the triangular defect, plating accumulates along the edges of the triangle, while its asymmetry makes plating more favorable along the longer edges than the shorter one. Figure 3a is a representative grayscale image of a graphite electrode upon disassembly, with white patches showing the metallic lithium. One of the experimental challenges is to deal with the statistical variations from cell to cell. To overcome this problem, we add images from multiple cells and normalize to generate an averaged image. This process provides us with the amount of plating at various locations in a more statistically robust manner. Figure 3b, which is created by taking 30 images of different cells, reveals that the majority of plating occurs along the edges with almost no plating around the 30-degree vertex.

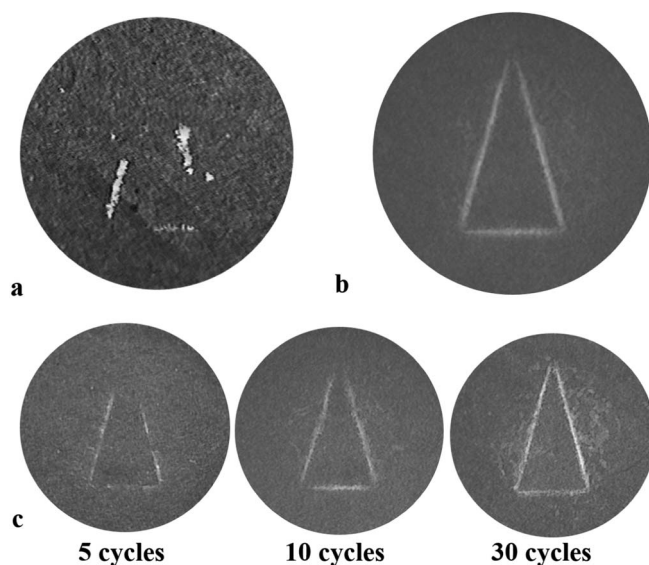


Figure 3. (a) A representative grayscale image of a graphite electrode showing localized plating due to a triangle-shaped defect. (b) An average of electrodes from 30 different cells showing that plating preferentially occurs around the edges and is unlikely to occur at the tip. (c) Averages of graphite electrodes from cells with 5, 10, and 30 cycles. Each image was averaged with a sample number from 5 to 8 different cells.

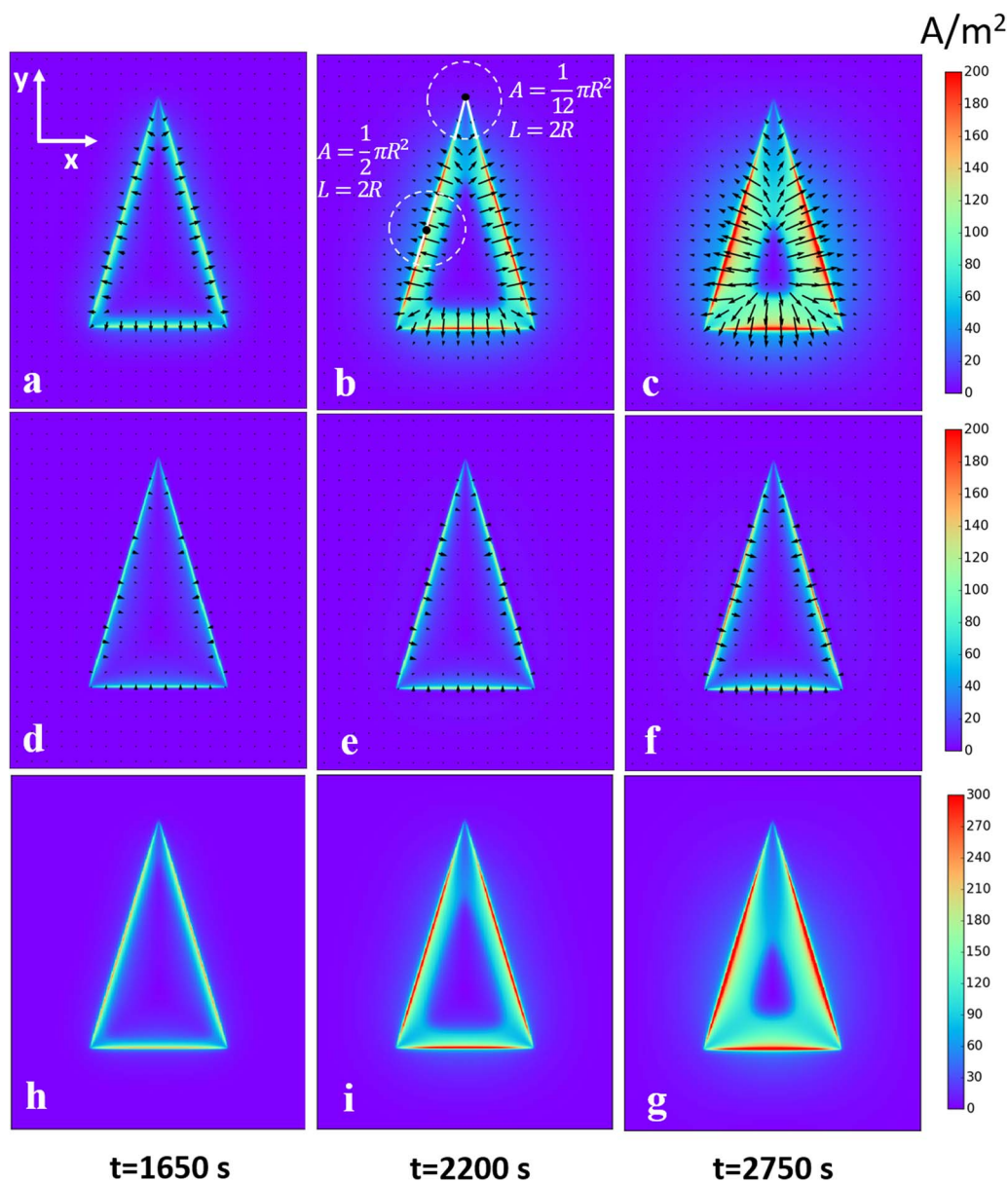


Figure 4. Lateral flux of lithium ions as indicated by the current density $\vec{i} = -\kappa_{eff} \vec{\nabla} \phi_2$ at the interface between the separator and the cathode (a-c), and between the separator and the anode (d-f) as time evolves from left to right. The black arrows are the x and y components of the flux vectors, with color bars indicating the magnitude. (h-g) The magnitude of differences between flux vectors at surfaces of two electrodes as time evolves, which is calculated as the magnitude of the vector difference of the x and y components.

Localized plating occurs due to unequal lateral transport in electrodes.¹⁵ Due to its smaller tortuosity, the lateral transport in the cathode (LCO) is faster than the transport in the anode (C).^{15,28–32} When the flux of the lithium transfer from the cathode exceeds the flux of lithium diffusion into the anode, lithium ions start to accumulate at the anode surface. Once the concentration of lithium ions at the surface reaches the saturation level, metallic lithium starts to form.^{9,33}

We use simulation results to help elucidate the localization effects due to defect geometry. We perform a 3D simulation of charging at 1C with a triangle-shaped defect. Figure 4 shows the lateral lithium ion current density flux vectors $\vec{i} = -\kappa_{eff} \vec{\nabla} \phi_2$ at the interfaces between the separator and each of the two electrodes, overlaid with a color map of the flux magnitude. Here we plot only the lateral (x and y) components of lithium ion fluxes at three different charging times. The asymmetry of the defect shape creates regions with non-uniform fluxes. Fluxes exiting the cathode are higher along edges than around vertices, while the fluxes entering the anode are smaller and more uni-

form. By plotting the magnitude of the difference of the fluxes, shown in Figures 4h–4g, we show that edges have a higher flux difference than the tip, and therefore it takes a shorter time for ions to accumulate and form metallic lithium there.

The variations in fluxes at the cathode can also be illustrated by considering the movement of ions. Let us refer to the ions in a region above a defect as “blocked ions”. Due to hindered direct transport induced by the separator pore closure, under an applied potential field, those “blocked ions” have to move laterally around the defect to get to the opposite electrode. The available area that allows those blocked ions to diffuse through is proportional to the length of the defect perimeter. Here we refer to the available area for diffusion as the exit and simplify it to a one-dimensional length. For instance, all the ions within the triangular area are blocked and the length of exit is the perimeter of the triangle.

Consider a region defined by the dashed circle with a radius of R as shown in Figure 4b. The amount of blocked ions within that circular

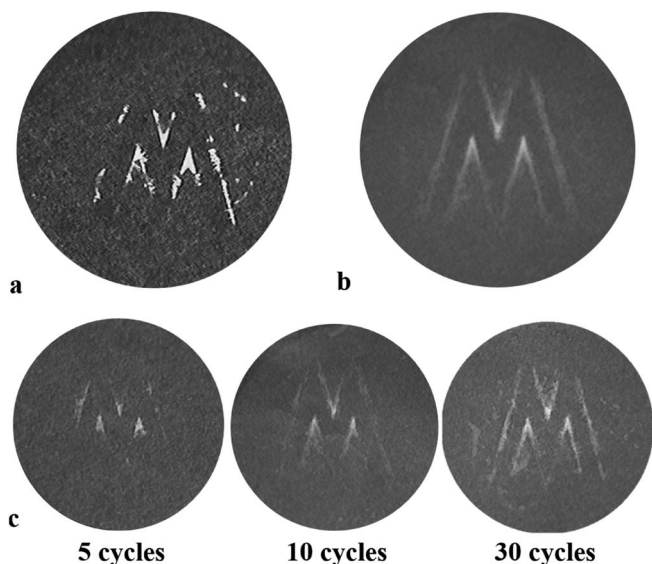


Figure 5. (a) A representative grayscale image of a graphite electrode showing localized plating due to an M-shaped defect. (b) An average of electrodes from 30 different cells showing that plating preferentially occurs at the inner vertices, followed by the edges, then the tips. (c) Averages of graphite electrodes from cells with 5, 10, and 30 cycles. Each image was averaged with a sample number from 5 to 8 different cells. Plating is likely to initiate at the inner vertices and gradually propagate around the edges.

region is proportional to the defect area, and the length of exit is the length of defect borders within that circle. Here we introduce an ion per exit ratio (*I/E* ratio) defined as

$$I/E = \frac{\text{Amount of Blocked Ions}}{\text{Exit}} = \frac{\text{Defect Area}}{\text{Border Length}} \quad [12]$$

which describes the level of crowding near the edge of the defect and can be calculated at each point on the edge. A larger *I/E* ratio indicates a higher degree of crowding, and therefore a higher probability of plating. In the examples given in Figure 4b, the *I/E* ratio is $\frac{1}{4}\pi R$ at the point on the edge, and is $\frac{1}{24}\pi R$ at the tip. These two points have the same length of exit, as indicated by white lines in Figure 4b, but the amount of blocked ions is much smaller at the tip, therefore resulting in a smaller *I/E* ratio. This matches our simulations that show that fluxes leaving from the cathode are smaller at the tip.

Compared to the triangular case, the inner vertices of the M-shaped defect create an even stronger effect. At the inner vertex, a large percentage of area is blocked by the pore closure, leading to a high *I/E* ratio with very concentrated ion flow. Performing a similar calculation as before yields an *I/E* ratio at the inner vertex of $\frac{11}{24}\pi R$. The fact that the *I/E* ratio is higher at the inner vertex than at the edge matches with our experimental observations as shown in Figure 5a. Plating is more likely to initiate around the inner vertices of a defect, followed by edges, then tips. Again, Figure 5b shows the statistically averaged plating locations on the negative electrode from 30 different cells.

Simulations show similar results as the experiments, which suggests that the model is able to infer the occurrence of plating. In Figure 6 we present results from 3D simulations of charging at 1 C for 2750 s with triangle-shaped and M-shaped pore closure defects. The most negative potential occurs at the center of the triangle edges and within the corners of the ‘M’, indicating greatest propensity for lithium plating in those locations. The overpotential at the longer edge of the triangle is more negative than that at the shorter edge, suggesting that simulations can provide information that is difficult to observe in experiments otherwise.

To probe how the plating propagates, we disassemble a number of cells after 5, 10, and 30 cycles. We record an image of the graphite

electrode from each cell and generate an averaged image for each cycle number. Each of the averaged images shown in Figure 3c and Figure 5c was produced from 5-8 samples. This series of images suggests that plating is nucleated at inner vertices and edges where the incoming fluxes are the highest, and gradually grows along the edge and radially outward. Localized plating is relatively continuous, because the dead lithium serves as a new defect, creating corner-like regions that induce concentrated ion flow. Using different defect geometries, we show that localization depends on the difference between transport in the cathode and anode as well as the *I/E* ratio.

The applied current density does not affect the spatial distributions imposed by defect geometry, but it will affect the overall tendency for plating in the same way as current density affects homogeneous plating. With an increased current density, which is equivalent to an increased flux leaving the cathode, while the *I/E* ratio remains the same, the fluxes increase everywhere and can now induce plating even at the tip. We experimentally observe that plating occurs uniformly around the edges of a defect at a higher C rate. In other words, the critical condition for plating correlates positively to the *I/E* ratio as well as the current density. A higher *I/E* ratio or current density makes a location more vulnerable to plating.

Localization and Defect Size

Simulation predictions.—In the previous section we showed that the *I/E* ratio of a defect determines locations where plating is likely to initiate in the case of various geometries and the *I/E* ratio should be minimized. Here we show that the *I/E* ratio can also help correlate plating to defect size. We perform 2D simulations of charging at 0.67 C in a cell with one small and one large rectangular stripe defect, as shown in Figure 7. The rectangular shape reduces model dimension and is also easier to implement experimentally. Here the *I/E* ratio can be represented as the area of rectangle over the length of two edges:

$$I/E \text{ ratio} = \frac{\text{Amount of Blocked Ions}}{\text{Exit}} = \frac{\text{Defect Area}}{\text{Border Length}} = \frac{LW}{2L} = \frac{W}{2} \quad [13]$$

where *L* is the length of the stripe, and *W* is the width that is equivalent to the defect size. A smaller defect leading to a smaller *I/E* ratio matches with the simulation result that after 4000 s of charging, the local potential drops below zero near the large defect but not the small defect, which suggests plating is less likely to occur around a smaller defect.

With the same amount of blocked ions, we can also increase the total length of exit to reduce the *I/E* ratio and consequently reduce the plating. Here, we perform 2D simulations of charging at 0.67 C in a cell with a collection of adjacent small defects and a continuous large defect with the same total closure area. As shown in Figure 8, lithium plating is favorable around the large continuous defect but not the collection of adjacent small defects. With small openings, we increase the length of exit, which significantly reduces plating. Note that this behavior only occurs for sufficiently small sizes of the small defects. When the width of the small defects is sufficiently large, plating will also occur in the gaps between the defects. Our simplified model works qualitatively well on a single defect or a series of small defects that were separated with a sufficiently large distance. Further studies and analysis are required to predict plating caused by defects that are more closely spaced as well as in other scenarios.

Experimental results.—We experimentally confirm that a single large defect induces more plating than a collection of smaller defects that have the same total area. Figure 9b compares plating along multiple small defects with plating along a 1.5 mm-wide defect. The small defects are 300 μm wide with 100 μm spacing in between, as shown in Figure 9a. The collection of small defects have the same total area as the 1.5 mm-wide defect, but induces no plating. In other words, if the effect of total defect area on the

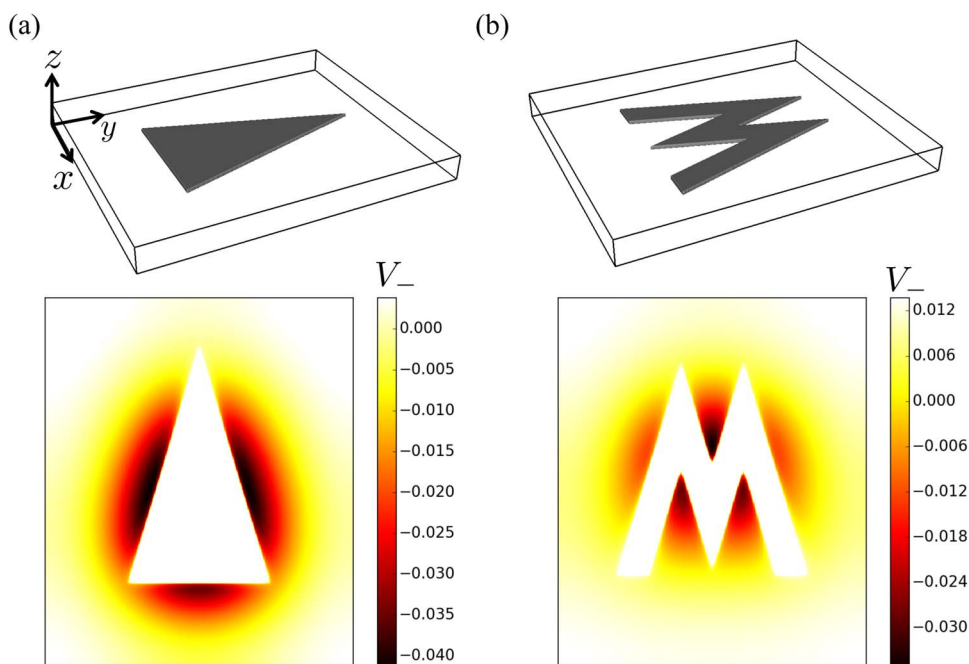


Figure 6. Region of pore closure (gray) in 3D simulations and local potential V_- at the surface of the anode for (a) a triangle-shaped defect or (b) an M-shaped defect. Colorbars are scaled for clarity, and the actual maximum value in the plot is larger than the maximum of the colorbar.

average current density is negligible, which is a valid assumption in practical situations when defects are small, it is the maximum defect size $A_{d,max}$ that determines plating, rather than the total defect area $A_{d,total}$.

As suggested from the simulations, the overpotential around a small defect never drops below 0 vs Li/Li^+ . Therefore, at each cur-

rent density, there should exist a critical size that triggers plating. Here, we quantitatively characterize the correlation between critical defect size and localized plating. In this experiment, a rectangular defect that has a width ranging from 50 μm to 1 mm, is placed inside a coin cell, along with a 1.5 mm wide defect which acts as a control. They are separated by 2 mm to avoid any interactions, as shown in Figure 10a. After

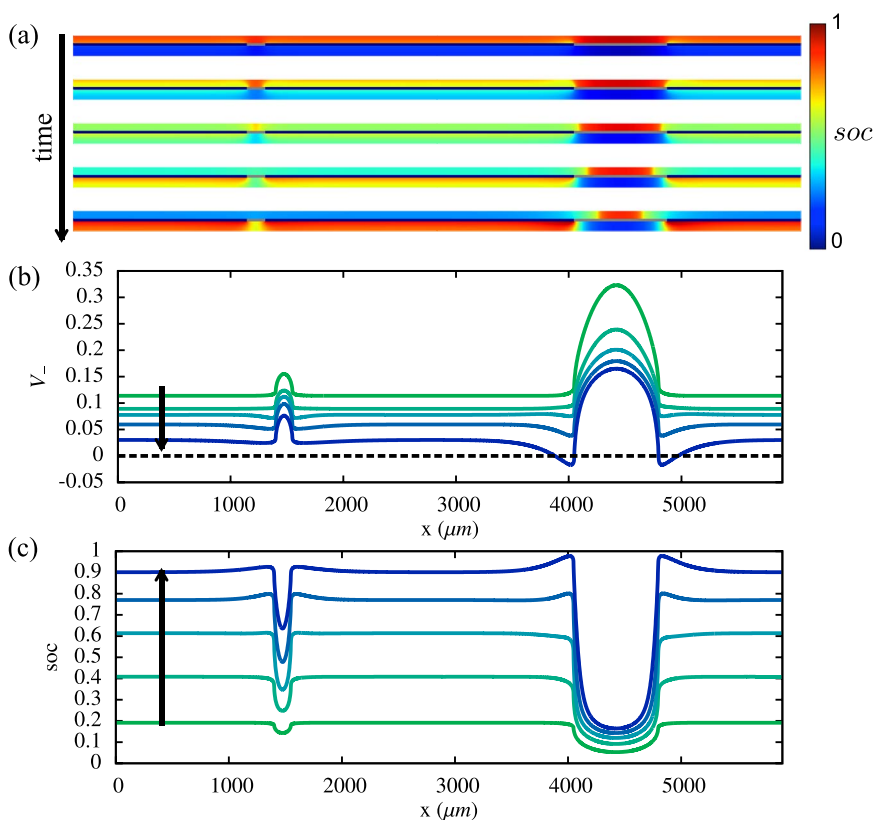


Figure 7. (a) Cross sections of local state of charge after 800 s, 1600 s, 2400 s, 3200 s, and 4000 s of charging. The top layer is the battery cathode, the bottom layer is the graphite anode, and the pore closure region is plotted in gray. (b) Potential V_- at the surface of the anode adjacent to the separator, at the same time snapshots as in (a). Lithium plating is favored near the large defect but not the small defect. (c) Local state of charge at the surface of the anode adjacent to the separator, at the same time snapshots as in (a).

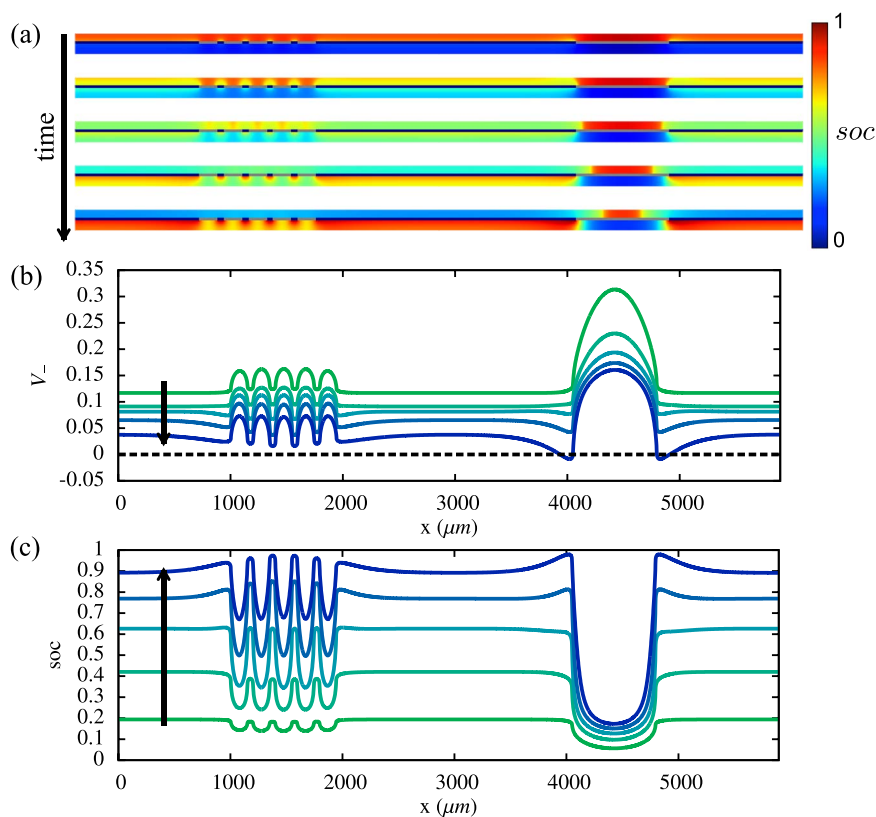


Figure 8. (a) Cross sections of local state of charge after 900 s, 1800 s, 2700 s, 3600 s, and 4500 s of charging. (b) Potential V_- at the surface of the anode adjacent to the separator, at the same time snapshots as in (a). Lithium plating is more likely adjacent to the large continuous defect than in the vicinity of the collection of small defects with the same total width. (c) Local state of charge at the surface of the anode adjacent to the separator, at the same time snapshots as in (a).

10, 20, and 50 cycles, cells were disassembled to observe any localized plating. Figure 10 shows representative images of graphite electrodes after 20 cycles, suggesting that localization is significantly reduced once the width of the defect drops below $400 \mu\text{m}$. Lithium plating is a complicated mechanism which can be affected by a number of factors, including the starting amount of lithium inventory in both electrodes, local current densities, and temperature.^{1, 12, 34, 35} Although parameters are all controlled, the heterogeneities and variations among cells have made experimental studies challenging. Therefore, a probability plot is obtained and presented in Figure 11, with the total sample numbers for each test summarized in Table II. There are two reasons for the observed increase in probability of plating as cycle number increases. First, as cycle number increases, lithium nuclei are more likely to grow and aggregate, and to be detected by the camera.^{36, 37}

Second, the plated dead lithium acts as a defect and increases the local stress which reduces the local porosity of the separator. This blocks additional pathways for ion transport, which increases the effective average current density and aggravates plating.³⁸ The critical defect size is shown to be below $400 \mu\text{m}$.

In this work, we fix the current density and identify a critical size for plating. However, note that the critical size should also depend on current density, temperature, as well as other properties of electrodes that affect transport. As current density increases, the critical defect size becomes smaller. Once the current density exceeds the homogeneous plating threshold, instead of nucleating on the defect edges, plating nucleates homogeneously in the bulk area. The argument of critical defect size also applies to the shape effect. At each point on the edge of a defect, there exists a critical I/E ratio which dictates the onset of plating. While it is important to point out that the critical defect size drops as current density increases, a full characterization based on current density is beyond the scope of this work.

Conclusions

In this paper, we experimentally demonstrate the geometry and size dependence of defects on localized plating in lithium-ion batteries. Through a simplified model, we show that transport non-uniformities cause fluxes to vary across the defect shape and lead to regions crowded with ions at the borders. Those regions correspond to spots where metallic plating is most often observed in experiments. By defining an ion to exit ratio (I/E ratio), which is a characteristic of the defect geometry and size, we relate that ratio to the propensity of plating. A smaller I/E ratio indicates a smaller probability of localized plating. Note that this simplified ion to exit ratio has only been demonstrated in the case of a single defect or a series of defects with sufficiently large spacing between them. We also demonstrated experimentally with supporting evidence from simulations that localization depends on the defect size. As the size of non-uniformities exceeds a critical level, lithium ions are more likely

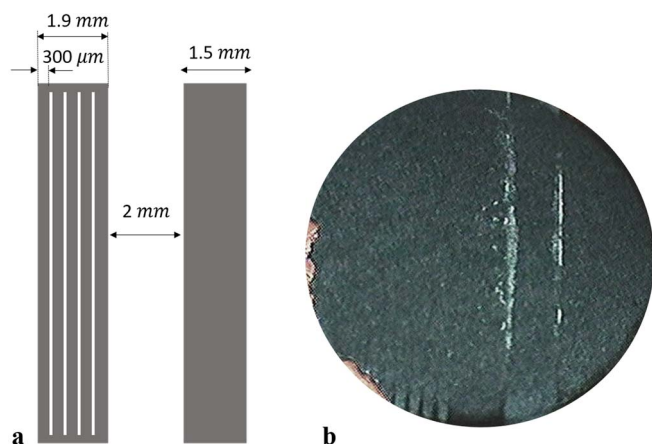


Figure 9. (a) Schematics of a large single defect and five small defects. (b) A representative image of a graphite electrode that shows localized plating along the large single defect but not along the multiple small defects, after 20 cycles at 0.67 C .

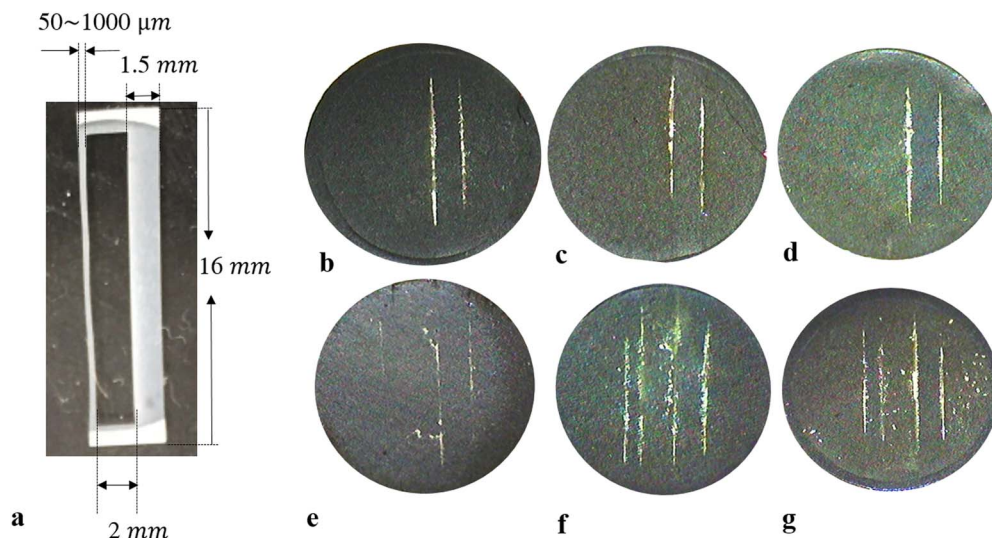


Figure 10. (a) Dimensions of a separator defect. (b-g) Representative images of plating along a 1.5 mm-wide defect compared to plating along a 50 μm (b), 200 μm (c), 400 μm (d), 600 μm (e), 800 μm (f), and 1 mm (g) wide defect on the graphite electrodes after 20 cycles at 0.67 C.

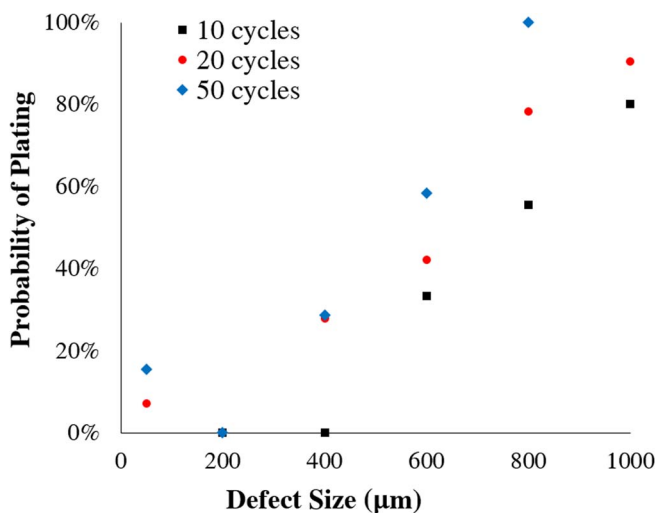


Figure 11. Probability of localized plating as a function of defect size after 10, 20 and 50 cycles. The overall probability of localized plating increases with cycle number.

to deposit as metallic lithium and form plating. Through increasing the total length of exit, we show that multiple small defects induce much less plating than a single continuous large defect that has the same total area.

Table II. Number of samples that show localized plating over the total sample numbers.

Defect Size (μm)	10 cycles	20 cycles	50 cycles
50	NA	1/14	2/13
200	0/3	0/16	0/13
400	0/4	5/18	4/14
600	2/6	8/19	7/12
800	5/9	18/23	4/4
1000	4/5	19/21	NA

Acknowledgments

This work is funded by National Science Foundation through Materials Research Science and Engineering Center (DMR-1420541). We acknowledge support from the PRISM Imaging and Analysis Center (IAC) and Micro/Nano Fabrication Laboratory (MNFL), as well as summer students, Jon Wilson and Anne-Marie Obiadi, who had contributed to this project. Alta Fang acknowledges the National Science Foundation Graduate Research Fellowship under grant No. DGE 1148900. We thank Semicorp Co. for providing us with thin separators. We thank CAMP (Cell Analysis, Modeling and Prototyping) Facility and Support group at Argonne National Laboratory for providing test electrodes.

Appendix

Here we present the model details. Since we assume that the solid-phase potential in each electrode is constant, the solid-phase potential in the cathode is $\phi_{1,+} = 0$, while throughout the anode, $\phi_{1,-} = -\phi_{\text{applied}}$. Here, the $-$ subscript refers to the anode and the $+$ subscript refers to the cathode.

The governing Equations 6–9 presented in the modeling methods section are reprinted here:

$$\varepsilon_s \frac{\partial c_s}{\partial t} = -aj; \quad [\text{A1}]$$

$$j\mathcal{F} = i_0(c, c_s, k) \frac{\mathcal{F}}{RT} (\phi_1 - \phi_2 - U(c_s)); \quad [\text{A2}]$$

$$aj\mathcal{F} = \vec{\nabla} \cdot (-\kappa_{\text{eff}} \vec{\nabla} \phi_2); \quad [\text{A3}]$$

$$0 = \vec{\nabla} \cdot (\kappa_{\text{eff}} \vec{\nabla} \phi_2). \quad [\text{A4}]$$

For our simulations, parameter values from Refs. 15 and 10 are used, which correspond to a lithium-ion battery with a graphite anode and Li_yCoO_2 cathode, as described in Table I. Here we use electrode potentials given by the following empirical formulas for Li_xC_6 and Li_yCoO_2 respectively:¹⁰ $U_-(x) = 0.7222 + 0.13868x + 0.028952x^{0.5} - 0.017189x^{-1} + 0.0019144x^{-1.5} + 0.28082e^{15(0.06-x)} - 0.79844e^{0.44649(x-0.92)}$ and $U_+(y) = 3.8552 + 1.2473(1-y) - 11.152(1-y)^2 + 42.8185(1-y)^3 - 67.711(1-y)^4 + 42.508(1-y)^5 - 6.132 \times 10^{-4} e^{7.657y^{115}}$, where $x = \frac{c_s}{c_{s,\text{max},-}}$ and $y = \frac{c_s}{c_{s,\text{max},+}}$. The effective conductivities in the electrodes and separator depend on the porosity and Bruggeman exponent via

$$\kappa_{\text{eff}} = \kappa \varepsilon_l^{\text{brugg}}. \quad [\text{A5}]$$

The exchange current density is modeled via

$$i_0(c, c_s, k) = \mathcal{F} k c^{0.5} (c_{s,\text{max}} - c_s)^{0.5} c_s^{0.5}. \quad [\text{A6}]$$

The boundary conditions at the edges of the cell are $\vec{\nabla}\phi_2 \cdot \hat{n} = 0$, where \hat{n} is the unit vector normal to the boundary, so that there is zero ionic current leaving the edges of the cell.

We first numerically solve Equations A2–A4 for ϕ_2 everywhere in the cell and then evolve c_s according to Equation A1 using explicit Euler time stepping. The equations are discretized on a uniform grid using finite difference methods. We use $N_x = 3360$ grid points in the plane of the electrodes and $N_z = 96$ grid points along the cell stack direction for 2D simulations. In our 3D simulations, we simulate only half of the cell due to the symmetry of the separator defect shapes and thus use $N_x = 240$, $N_y = 576$, $N_z = 48$ grid points, where the full cell is reconstructed by mirroring in the x direction. The sparse matrix equation for ϕ_2 at each time step is solved using the PETSc software package. We model a constant applied current by using an iterative bisection scheme to solve at each time step for the cell potential $\phi_{applied}$ such that the total current in the cell is within an error tolerance factor of 2.5×10^{-3} of the target current.³⁹ Estimates for the cell potential $\phi_{applied}$ for the next step are made using linear extrapolation based on the cell potential from the previous and current time steps, and the window of estimated potential input into the bisection algorithm is $\pm 0.0005V$. Total current I in the cell is calculated by integrating the normal component of the current density over the area of the cell in a cross-section in the separator just above the anode via $I = -\int \kappa_{eff} \frac{\partial \phi_2}{\partial z} dA$. Reported values of applied current are given in terms of C-rate, where the C-rate is calculated with a geometric factor accounting for the pore closure area, which assumes that there is no capacity contribution from the electrode material directly above or below the pore closure.¹⁵

ORCID

Craig B. Arnold  <https://orcid.org/0000-0002-0293-5411>

References

- J. Vetter, P. Novák, M. Wagner, C. Veit, K.-C. Möller, J. Besenhard, M. Winter, M. Wohlfahrt-Mehrens, C. Vogler, and A. Hammouche, *J. Power Sources*, **147**, 269 (2005).
- P. Arora, R. E. White, and M. Doyle, *J. Electrochem. Soc.*, **145**, 3647 (1998).
- J.-M. Tarascon and M. Armand, in *Materials For Sustainable Energy: A Collection of Peer-Reviewed Research and Review Articles from Nature Publishing Group* (World Scientific, 2011) pp. 171–179.
- P. Bai, J. Li, F. R. Brushett, and M. Z. Bazant, *Energy & Environmental Science*, **9**, 3221 (2016).
- A. Jana, D. R. Ely, and R. E. García, *J. Power Sources*, **275**, 912 (2015).
- Z. Li, J. Huang, B. Y. Liaw, V. Metzler, and J. Zhang, *J. Power Sources*, **254**, 168 (2014).
- M. Petzl, M. Kasper, and M. A. Danzer, *J. Power Sources*, **275**, 799 (2015).
- C. von Lüders, V. Zinth, S. V. Erhard, P. J. Osswald, M. Hofmann, R. Gilles, and A. Jossen, *Journal of Power Sources*, **342**, 17 (2017).
- P. Arora, M. Doyle, and R. E. White, *J. Electrochem. Soc.*, **146**, 3543 (1999).
- M. Tang, P. Albertus, and J. Newman, *J. Electrochem. Soc.*, **156**, A390 (2009).
- C. Uhlmann, J. Illig, M. Ender, R. Schuster, and E. Ivers-Tiffée, *J. Power Sources*, **279**, 428 (2015).
- J. Burns, D. Stevens, and J. Dahn, *J. Electrochem. Soc.*, **162**, A959 (2015).
- M. Petzl and M. A. Danzer, *J. Power Sources*, **254**, 80 (2014).
- B. Bitzer and A. Gruhle, *J. Power Sources*, **262**, 297 (2014).
- J. Cannarella and C. B. Arnold, *J. Electrochem. Soc.*, **162**, A1365 (2015).
- A. H. Zimmerman and M. V. Quinzio, in *Presented at the NASA Battery Workshop*, Vol. 16, p. 18 (2010).
- T. C. Bach, S. F. Schuster, E. Fleder, J. Müller, M. J. Brand, H. Lorrman, A. Jossen, and G. Sextl, *Journal of Energy Storage*, **5**, 212 (2016).
- J. Cannarella and C. B. Arnold, *J. Power Sources*, **245**, 745 (2014).
- J. B. Siegel, A. G. Stefanopoulou, P. Hagans, Y. Ding, and D. Gorsich, *Journal of the Electrochemical Society*, **160**, A1031 (2013).
- J. Cannarella, X. Liu, C. Z. Leng, P. D. Sinko, G. Y. Gor, and C. B. Arnold, *J. Electrochem. Soc.*, **161**, F3117 (2014).
- Y.-T. Cheng and M. W. Verbrugge, *Journal of Power Sources*, **190**, 453 (2009).
- C. Peabody and C. B. Arnold, *J. Power Sources*, **196**, 8147 (2011).
- J. Cannarella and C. B. Arnold, *J. Power Sources*, **226**, 149 (2013).
- T. F. Fuller, M. Doyle, and J. Newman, *J. Electrochem. Soc.*, **141**, 1 (1994).
- S. Allu, S. Kalnaus, S. Simunovic, J. Nanda, J. A. Turner, and S. Pannala, *J. Power Sources*, **325**, 42 (2016).
- R. D. Perkins, A. V. Randall, X. Zhang, and G. L. Plett, *J. Power Sources*, **209**, 318 (2012).
- R. Purkayastha and R. M. McMeeking, *Journal of Applied Mechanics*, **79**, 031021 (2012).
- K. Kumaresan, G. Sikha, and R. E. White, *J. Electrochem. Soc.*, **155**, A164 (2008).
- K. Persson, V. A. Sethuraman, L. J. Hardwick, Y. Hinuma, Y. S. Meng, A. van der Ven, V. Srinivasan, R. Kostecki, and G. Ceder, *The journal of physical chemistry letters*, **1**, 1176 (2010).
- D. K. Karthikeyan, G. Sikha, and R. E. White, *J. Power Sources*, **185**, 1398 (2008).
- B. Wang, J. Bates, F. Hart, B. Sales, R. Zuhr, and J. Robertson, *J. Electrochem. Soc.*, **143**, 3203 (1996).
- S. J. Harris, A. Timmons, D. R. Baker, and C. Monroe, *Chemical Physics Letters*, **485**, 265 (2010).
- B. Purushothaman and U. Landau, *J. Electrochem. Soc.*, **153**, A533 (2006).
- T. Waldmann, M. Wilka, M. Kasper, M. Fleischhammer, and M. Wohlfahrt-Mehrens, *J. Power Sources*, **262**, 129 (2014).
- V. Zinth, C. von Lüders, M. Hofmann, J. Hattendorff, I. Buchberger, S. Erhard, J. Rebelo-Kornmeier, A. Jossen, and R. Gilles, *J. Power Sources*, **271**, 152 (2014).
- D. R. Ely and R. E. García, *J. Electrochem. Soc.*, **160**, A662 (2013).
- A. Pei, G. Zheng, F. Shi, Y. Li, and Y. Cui, *Nano letters*, **17**, 1132 (2017).
- X.-G. Yang, Y. Leng, G. Zhang, S. Ge, and C.-Y. Wang, *J. Power Sources*, **360**, 28 (2017).
- S. DeWitt, N. Hahn, K. Zavadil, and K. Thornton, *J. Electrochem. Soc.*, **163**, A513 (2016).